

IED command wire detection using multi-aspect processing on SAR images

Klein, K.T.J.; Uysal, Faruk; Caro Cuenca, Miguel; Otten, Matern; de Wit, TNO

DOI

[10.1109/RadarConf2043947.2020.9266662](https://doi.org/10.1109/RadarConf2043947.2020.9266662)

Publication date

2020

Document Version

Final published version

Published in

2020 IEEE Radar Conference, RadarConf 2020

Citation (APA)

Klein, K. T. J., Uysal, F., Caro Cuenca, M., Otten, M., & de Wit, TNO. (2020). IED command wire detection using multi-aspect processing on SAR images. In *2020 IEEE Radar Conference, RadarConf 2020* (pp. 1559-1564). Article 9266662 (IEEE National Radar Conference - Proceedings; Vol. 2020-September). IEEE. <https://doi.org/10.1109/RadarConf2043947.2020.9266662>

Important note

To cite this publication, please use the final published version (if applicable).
Please check the document version above.

Copyright

Other than for strictly personal use, it is not permitted to download, forward or distribute the text or part of it, without the consent of the author(s) and/or copyright holder(s), unless the work is under an open content license such as Creative Commons.

Takedown policy

Please contact us and provide details if you believe this document breaches copyrights.
We will remove access to the work immediately and investigate your claim.

IED Command Wire Detection using Multi-Aspect Processing on SAR Images

Keith T.J. Klein^{*†}, Faruk Uysal^{*}, Miguel Caro Cuenca[†], Matern P.G. Otten[†] and Jacco J.M. de Wit[†]

^{*}*Microwave Sensing, Signals and Systems, Delft University of Technology, Delft, The Netherlands*

[†]*Department of Radar Technology, TNO, The Hague, The Netherlands*

Email: k.t.j.klein@student.tudelft.nl

Abstract—In this paper, a wire detection algorithm is proposed for synthetic aperture radar (SAR) images. The algorithm is specifically designed for SAR images generated from an agile, drone-mounted, omnidirectional radar array to be used for the detection of improvised explosive devices (IEDs). A multistage approach consisting of denoising, constant false alarm rate (CFAR) thresholding, feature extraction, and automated detection using the Radon transform, is proposed and applied to a set of SAR images with multiple aspect angles. At each detection step, the look-angles of individual pixels are used to remove false alarms, and improve detection accuracy. The algorithm is tested using measured data and provides an acceptable detection performance on straight wire segments even in the presence of a strong background clutter.

I. INTRODUCTION

The conventional methods of detection for improvised explosive devices (IEDs) are slow and potentially dangerous. Since radio-controlled IEDs can be counteracted using jammer systems, most IEDs resort to command wires for detonation. Because of this, IEDs must be manually detected using hand-held devices or vehicle-mounted devices. Specialized airborne sensor systems exist to aid with the removal of IEDs. However, these are not easily deployable in many scenarios.

Different radar systems for the detection of landmines and IEDs have been proposed in recent literature [1]–[3]. Recent systems are based on unmanned aerial vehicles (UAVs) due to their ease of deployability, and usually exploit ground penetrating radar (GPR) to directly detect buried explosives. Another approach is the detection of IEDs through the presence of command wires. Since large parts of these wires are above ground, it is possible to use higher frequencies for imaging, leading to a compact payload. In [4], the detectability of IED command wires is investigated using ground-based synthetic aperture radar (SAR). An airborne, drone-based SAR system for the detection of thin metallic tripwires is presented in [5] which highlights the importance of imaging from multiple aspect angles, as well as the need for an accurate positioning system.

Wires can be relatively difficult to detect using radar, as the radar cross section (RCS) of a wire-segment decreases sharply when illuminated from oblique angles [6]. Therefore, a wide field-of-view, and imaging from multiple aspect angles

is necessary for good detection performance. Moreover, as command wires are relatively thin, the signal-to-clutter ratio (SCR) may be too low to spot the intended targets through visual inspection, even after constant false alarm rate (CFAR) detection. This is highlighted in [7], where an algorithm for the detection of power lines in polarimetric SAR images is proposed. In [8], the phase signature along specific wire orientations is exploited using a spatial frequency domain filter.

At TNO, an innovative multichannel omnidirectional SAR system has been developed for mini-UAV/drone platforms [9]. This compact SAR system consists of two circular, multilayer circuit boards with horizontal dipole antennas along the edges. The transmitter board comprises 16 elements, that can be switched on and off separately to shape the transmit beam. The receiver board comprises 32 elements which are digitized individually allowing full digital beamforming on receive. Metal discs are placed in between and over the circuit boards to provide transmit/receive isolation and elevation beam shaping. The complete system, shown in Fig. 1, weighs approximately 800 grams including the battery and has a maximum diameter of 25 cm. The system is based on the frequency modulated continuous wave radar principle and operates in X-band. The bandwidth is 1 GHz.



Fig. 1: The omnidirectional SAR system mounted on a drone.

Because of its wide field-of-view, the presented SAR system can serve as an ideal platform for the detection of IED command wires through SAR imaging. Backprojection applied

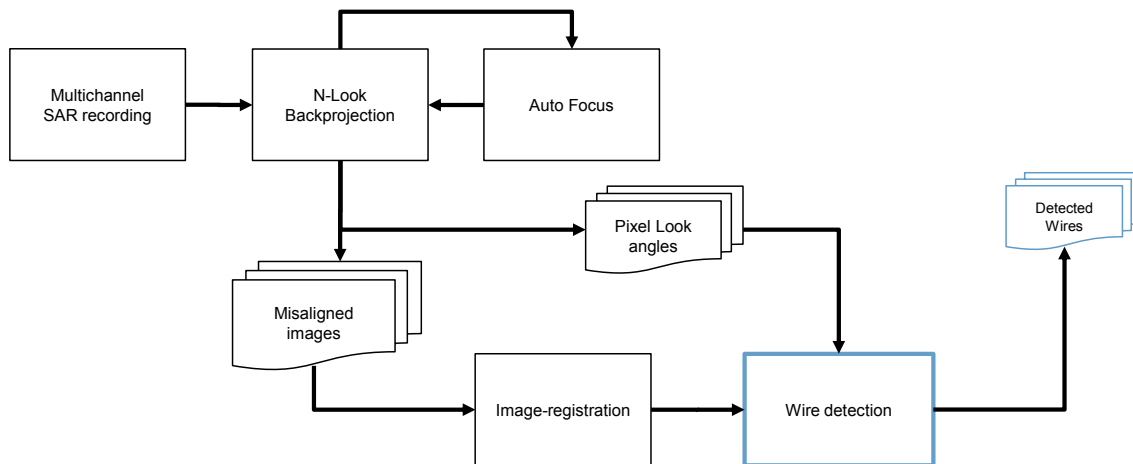


Fig. 2: Top level flowchart of the processing chain. The proposed wire detection block is highlighted in blue. This block is detailed in Fig. 3.

to subsequent subsets of receive channels implicitly performs beam steering and produces a set of SAR images of the targeted area with different aspect angles. The difference between the aspect angles, or look-angles, is chosen such that the subsequent synthetic apertures overlap. As a consequence, a wire segment yields a high RCS in at least one of the SAR images, i.e., the SAR image with look-angle perpendicular to the orientation of the wire segment. Note that a curved wire will be highlighted in several SAR images.

In this paper, we propose a multistage automated wire detection method that exploits the specifics of the omnidirectional SAR system. False alarms are minimized by taking into account the properties of wire returns from multiple look angles. Using image processing techniques applied in an adaptive manner, the algorithm extracts the location and length of potential wire segments in the SAR images.

The rest of the paper is organized as follows: The data set and collection geometry is presented in the next section. This is followed by an overview of the proposed algorithm. Finally, the detection results are compared to the ground-truth wire locations followed by a short conclusion.

II. SAR DATA SET

For the creation of SAR images, a subset of transmit and receive antennas are used in order to operate the radar in a side-looking mode. At an altitude of ~ 15 m, the drone flies along a straight trajectory at a distance of ~ 40 m to the scene center while the data are captured. The collected data are processed using a backprojection algorithm in combination with autofocusing to create a set of SAR images with different aspect angles. The imaging algorithm also generates a set of “maps” indicating the average look-angle of each pixel in each SAR image.

After the SAR images are generated, an image registration algorithm is used to align the images. The aligned images, as well as the look-angle map for each image, are used as an

input to the detection algorithm. A top-level flowchart of the processing chain can be seen in Fig. 2.

III. PROPOSED METHOD

The proposed wire detection algorithm is depicted in the flowchart in Fig. 3. As seen from the flowchart, the algorithm has two inputs; namely, coregistered SAR images and their associated look-angle maps. Fig. 4 shows the sum of all SAR images (after coregistration) taken from different aspect angles. The associated look-angle map of a single SAR image is presented in Fig. 5.

In the upcoming processing steps, images and look-angle maps will be defined by the functions

$$f(\mathbf{x}, i) | \mathbf{x} \in X \wedge i \in I \quad (1)$$

and

$$L(\mathbf{x}, i) | \mathbf{x} \in X \wedge i \in I, \quad (2)$$

respectively. Where the vector \mathbf{x} denotes the x, y coordinate, and i denotes the image number. Furthermore, to make it clear which step in the processing chain is being addressed, a subscript will be added to the function f . Therefore, $f_k(\mathbf{x}, i)$ denotes the pixel value of the i^{th} image at position \mathbf{x} after the k^{th} processing step.

A. Noise Filtering

To reduce the effect of speckle noise in the images, a noise filter is used. A simple approach for speckle noise filtering could be to average between multiple images. However, this leads to a loss of information, since each image has a unique look-angle map which is useful to determine wire returns. A filter which has been shown to provide adequate smoothing while preserving edges is the non-local means filter [10]. The non-local means filter replaces a target pixel with a weighted average of the mean of all pixels in the image. When filtering a certain pixel, the weight of every other pixel is determined by the similarity between its neighborhood, and the neighborhood

of the pixel under test. The filter is applied separately to each backprojected SAR image. The effect of the filter on one of the data sets can be seen in Fig. 6.

B. Adaptive Cell Averaging CFAR Detection

As an initial screening step, a cell averaging CFAR (CA-CFAR) detector is used. The CFAR guard window is line shaped to improve the detection of wire-shaped returns. Since the strongest reflection is expected at perpendicular illumination [6], the CFAR window is made adaptive in the sense that it rotates to be perpendicular to the angle defined in the look-angle map. To achieve this, the image is first divided into a number of angle segments by dividing the range of L into a number of subranges.

Given the i^{th} image and its look-angle map, its n^{th} segment is given by

$$f_{1,n}(\mathbf{x}, i) = \begin{cases} f_1(\mathbf{x}, i), & \text{for } \theta_n - \delta < L(\mathbf{x}, i) < \theta_n + \delta \\ 0, & \text{otherwise,} \end{cases} \quad (3)$$

where θ_n is the average look-angle, and δ is used to define the interval of angles belonging to a single segment. Each segment is then convolved with a different CFAR window with an orientation perpendicular to θ_n . The output from each segment is then summed to obtain the final clutter estimate. An illustration of this principle can be seen in Fig. 7.

The clutter estimate is divided by the original image pixel value in order to obtain the SCR. The SCR images are thresholded based on the expected SCR of wire returns (this depends on the scene being imaged).

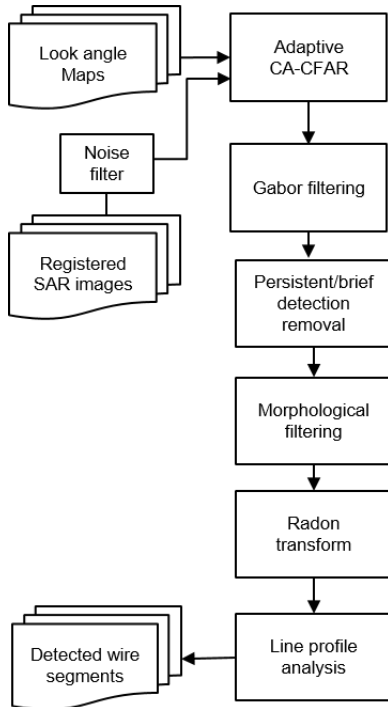


Fig. 3: Wire detection algorithm flowchart.

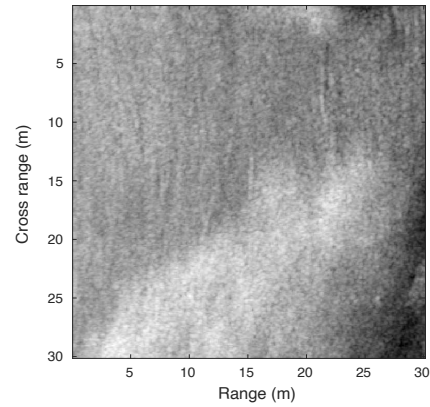


Fig. 4: The sum of 28 coregistered SAR images. The image is displayed in dB.

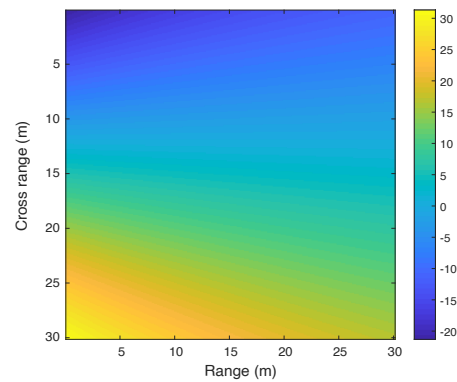


Fig. 5: An example of the look-angle map of associated with a single SAR image from the sum shown in Fig. 4. The angles correspond to the average look-angle of the radar during the imaging of a certain pixel.

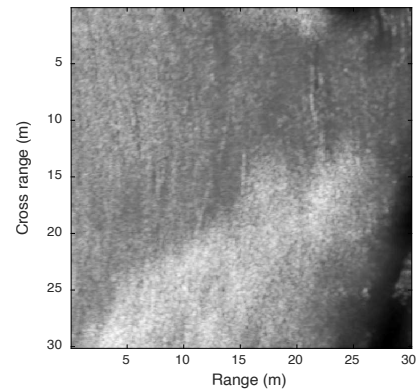


Fig. 6: The set of SAR images after non-local means filtering (for speckle noise reduction). Each image has been filtered individually. However, the sum is shown for illustration.

C. Gabor Filtering

After CFAR detection, there are usually still many false alarms present because of the relatively weak reflections from

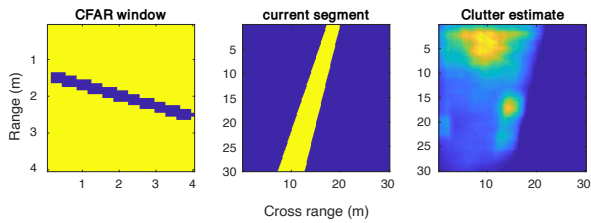


Fig. 7: Illustration of clutter estimation. The CFAR window is shown on the left side, the middle figure shows the current image segment in yellow, and on the right the running sum of all segments is illustrated.

wire segments. To further separate potential wire segments from clutter returns, a Gabor filter is used. The filter can be described by a Gaussian kernel modulated with a complex sinusoid

$$h(x, y) = e^{j(2\pi \frac{x_r}{\lambda_x} + \psi)} e^{-\frac{x_r^2 + \gamma^2 y_r^2}{2\sigma^2}}, \quad (4)$$

where $x_r = x \cos \theta + y \sin \theta$, $y_r = -x \sin \theta + y \cos \theta$, λ_x is the wavelength of the modulating sinusoid and γ and σ are the aspect ratio and standard deviation of the Gaussian envelope respectively. The parameter θ determines the orientation of the filter.

By using a bank of filters with different orientations, it is possible to determine the presence and location of specific spatial frequency components in an image. This is commonly used for image processing applications such as edge detection and fingerprint recognition [11], [12]. For this application however, a separate filter is applied to each image segment as defined in (3). This is done to suppress the returns from pixels which are aligned in unexpected orientations. The filters are oriented such that they are perpendicular to the average look-angle of their corresponding segment. Additionally, only the real part of the Gabor filter is used. This is because the features of interest are lines, which are symmetric features. The parameters of the filters are empirically chosen based on experiments with the data set. In Fig. 8, the chosen Gabor kernel can be seen.

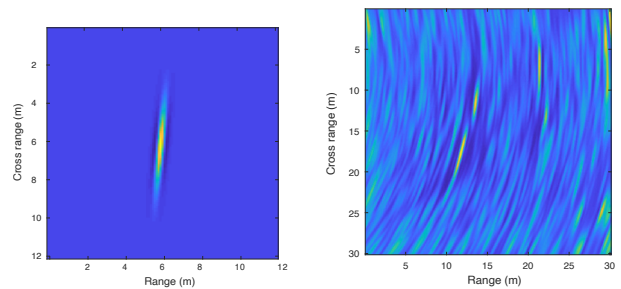
The CFAR detections are filtered based on a threshold, η_{gb} , applied to the output of the filter

$$f_3(\mathbf{x}, i) = \begin{cases} f_2(\mathbf{x}, i), & \text{for } g(\mathbf{x}, i) > \eta_{gb} \\ 0, & \text{otherwise,} \end{cases} \quad (5)$$

where g is the output of the Gabor filter. Fig. 9 shows the detections after filtering.

D. Connected Component Labeling

Another behavior of wire returns that can be exploited, is their short persistence over multiple look-angles. This means that given a certain detection, if it persists in the same location over an angle interval greater than some threshold, it can be determined that this detection does not originate from a wire but from some other strong reflector. This can be observed in Fig. 10, where a data set with many persistent targets is



(a) Gabor spatial kernel.

(b) Gabor filter output.

Fig. 8: Illustration of a) the Gabor spatial kernel and b) its output after convolution with the CFAR detections.

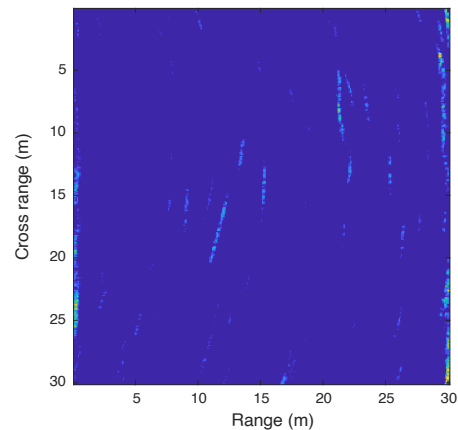


Fig. 9: The sum of detections after thresholding with the Gabor filter.

used to illustrate this principle. By generalizing the notion of adjacency of pixels as given in [13] to 3D images, we define the "persistence" of any given detection in the following way:

- Given the set of thresholded images $f_3(X, I)$, the pixel values of each image can be considered as voxels in a 3D array. All voxels are grouped based on their connectivity. Voxels connected by face or edge are considered to be a single three-dimensional detection.
- The persistence, θ_p , of each detection is then calculated by determining the interval of look-angles spanned by the detection.

When an interval of acceptable persistence values is defined, the detections outside of this interval can be discarded or labeled for further analysis.

E. Morphological Filtering

To further enhance wire-like detections and filter out unwanted detections, A number of morphological operations are applied [13]. This will reduce noise when applying the Radon transform in later steps. The operations are applied in the following order:

- 1) The image is divided into angle segments as defined in (3). Using a set of line-shaped structuring elements, a

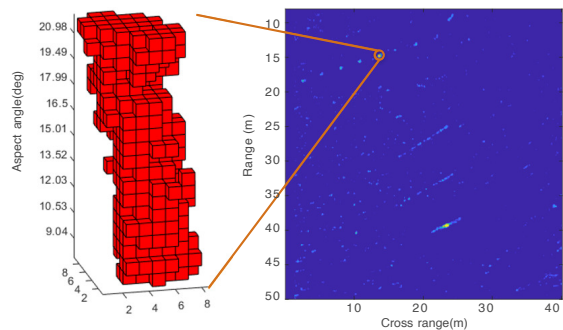


Fig. 10: An example of persistent target labeling: strong, stationary targets are easily detected and labeled.

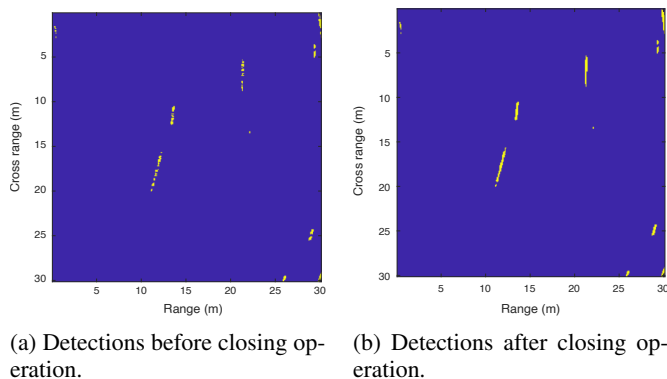


Fig. 11: This figure shows the effect of the closing operation performed on a single image in the data set.

morphological closing is performed on each segment. This has the effect of connecting pixels which are aligned in the expected orientation for wire returns, as shown in Fig. 11.

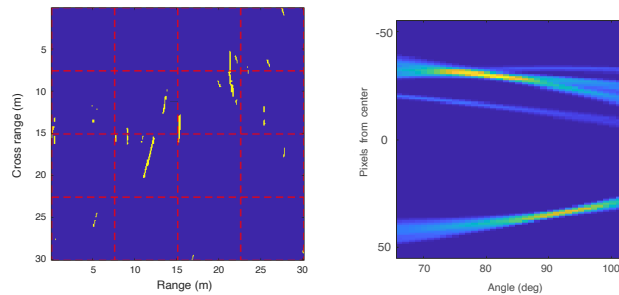
- 2) Extended targets are identified using a series of closings, openings and morphological reconstructions using square structuring elements of varying sizes. The output of these operations yields a template for unwanted detections in the images. These are then removed using a pixel-wise XOR operation.

After morphological filtering, the final images are summed up and thresholded to a single binary image.

F. Line Segment Detection using the Radon Transform

For automated detection of potential wire segments in the final image, the Radon transform is used [13]. The Radon transform maps a function defined on the x,y -plane to a function defined on the θ,ρ plane. where θ and ρ parameterize a line l on the x,y -plane. More specifically, ρ is the distance of l from the origin and θ is the angle that the normal vector of l makes with the x -axis. The two-dimensional Radon transform is expressed by

$$Rf_5(\theta, \rho, i) = \int_{-\infty}^{\infty} f_5((z \sin \theta + \rho \cos \theta), (-z \cos \theta + \rho \sin \theta), i) dz, \quad (6)$$



(a) Division of detections into separate blocks. (b) The Radon transform of a single image block.

Fig. 12: This figure shows the subimages and the result of applying the Radon transform to such a subimage.

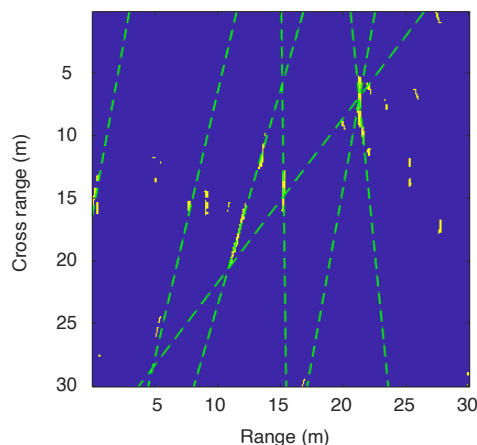


Fig. 13: The dashed lines show the potential wires obtained after the Radon transform. The actual location and length of a wire segment is found by analyzing the image profile along the related dashed line.

where p is the original function defined on the x,y -plane. A single line with angle θ and distance from the origin ρ is mapped to a single point on the Radon parameter space, with value equal to the sum of pixels along the line. Peaks in the Radon parameter space can therefore be used to detect the location of lines in an image.

Before applying the Radon transform, images are first subdivided into smaller blocks, see Fig. 12. This is done to minimize peaks caused by a summation of clutter pixels across the entire image. The Radon transform is then applied to each block separately. Peaks in the Radon transform represent the orientation and approximate location of potential wire segments as shown in Fig. 13. The length of a detected wire segment is determined by analyzing the profile along the line parameterized by the peak. The final wire segments are then constructed by combining detected segments from each image block. The detected wire segments can be seen in Fig. 14.

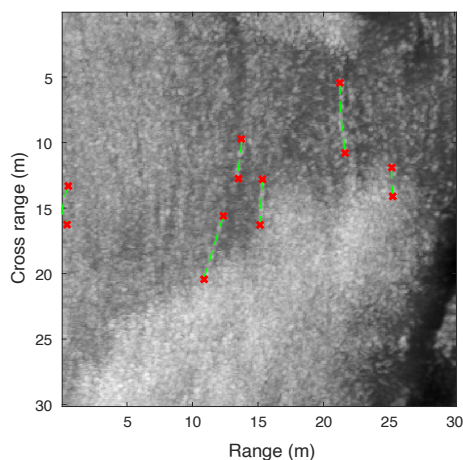


Fig. 14: The wire segments detected by the Radon transform.

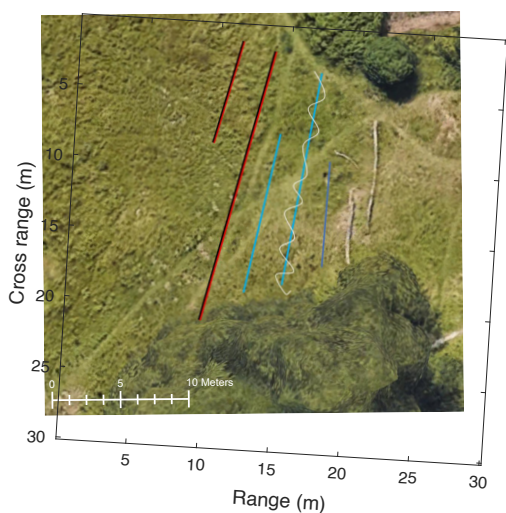


Fig. 15: The actual wire locations positioned in the scene. The outline of the SAR image shows the relative rotation between the two images.

IV. RESULTS

The output of the detection algorithm for a scene with multiple wire segments at different orientations can be seen in Fig. 14

The wires detected by the algorithm are parts of the straight red/black and blue wire as shown in Fig. 15. Returns from other segments are either not illuminated properly or over-powered by clutter returns. From the detections in Fig. 14, it can be seen that the tree trunks lying on the ground on the right side of the image are also detected as a wire return due to similar behavior.

V. CONCLUSION

This paper presented an automated wire detection algorithm for a set of SAR images with different aspect angles. By exploiting the spatial resolution of a SAR image, the detection algorithm can adequately detect long, straight wire segments

of approximately 5 m, providing an indication of potential IED devices in close proximity. In the presence of strong clutter, wires are still detectable. However, the minimum detectable length increases, as more pixels are required to find line features in the image. False alarms caused by objects with similar behavior can pose a problem for automated detection. These can be identified by either cross-referencing with a map of the environment or images from an on-board camera sensor.

The detection algorithm can be improved by performing multiple passes along a given area of interest to suppress random clutter. Incorporating data gathered from the other side of the wire segment would also increase SCR. In practical scenarios, full 360 degrees imaging of the area of interest would be desirable. Furthermore, to make the algorithm more robust, it would also be useful to establish some relationship between the imaging conditions and the detection parameters.

ACKNOWLEDGMENT

The development of this sensor is performed under U.S. Grants 12119916, and 12568517, from the Office of Naval Research, Expeditionary Maneuver Warfare Department.

REFERENCES

- [1] M. Schartel, R. Burr, W. Mayer, N. Docci, and C. Waldschmidt, "UAV-based ground penetrating synthetic aperture radar," in *2018 IEEE MTT-S International Conference on Microwaves for Intelligent Mobility (ICMIM)*, April 2018, pp. 1–4.
- [2] A. Goad, D. Schorer, J. Sullenberger, F. Yousuf, A. Yu, G. Donohue, and K. Hintz, "Landmine detection utilizing an unmanned aerial vehicle," in *2008 IEEE Systems and Information Engineering Design Symposium*, April 2008, pp. 231–236.
- [3] E. Schreiber, A. Heinzl, M. Peichl, M. Engel, and W. Wiesbeck, "Advanced buried object detection by multichannel, UAV/drone carried synthetic aperture radar," in *2019 13th European Conference on Antennas and Propagation (EuCAP)*, March 2019, pp. 1–5.
- [4] A. Heinzl, M. Peichl, E. Schreiber, S. Dill, and F. Bischeltstrieder, "The detection of IEDs using ground based multi-static SAR," in *2019 20th International Radar Symposium (IRS)*, June 2019, pp. 1–6.
- [5] M. Schartel, R. Burr, W. Mayer, and C. Waldschmidt, "Airborne tripwire detection using a synthetic aperture radar," *IEEE Geoscience and Remote Sensing Letters*, vol. 17, no. 2, pp. 262–266, Feb. 2020.
- [6] G. N. Crisp, C. R. Thornhill, and G. Gooding-Williams, "Detection of wires using UWB radar," in *Ultra-Wideband, Short-Pulse Electromagnetics 6*. Boston, MA: Springer US, 2003, pp. 471–480.
- [7] K. Sarabandi, L. Pierce, Y. Oh, and F. T. Ulaby, "Power lines: radar measurements and detection algorithm for polarimetric SAR images," *IEEE Transactions on Aerospace and Electronic Systems*, vol. 30, no. 2, pp. 632–643, April 1994.
- [8] J. K. Jao and S. Ayasli, "SAR detection of wires using image phase signatures," in *Proceedings International Radar Conference*, May 1995, pp. 362–368.
- [9] M. P. G. Otten, A. P. M. Maas, R. Bolt, M. Caro-Cuenca, and H. Medenblik, "Circular micro-SAR for mini-UAV," in *2018 15th European Radar Conference (EuRAD)*, Sep. 2018, pp. 321–324.
- [10] A. Buades, B. Coll, and J. Morel, "A non-local algorithm for image denoising," in *2005 IEEE Computer Society Conference on Computer Vision and Pattern Recognition (CVPR'05)*, vol. 2, June 2005, pp. 60–65 vol. 2.
- [11] K. R. Namuduri, R. Mehrotra, and N. Ranganathan, "Edge detection models based on Gabor filters," in *Proceedings, 11th IAPR International Conference on Pattern Recognition. Vol. III. Conference C: Image, Speech and Signal Analysis*, 1992, pp. 729–732.
- [12] A. K. Jain, S. Prabhakar, L. Hong, and S. Pankanti, "Filterbank-based fingerprint matching," *IEEE Transactions on Image Processing*, vol. 9, no. 5, pp. 846–859, 2000.
- [13] R. C. Gonzalez, *Digital Image Processing (4th Edition)*. Pearson, Mar. 2017.